Organic Electronics 35 (2016) 33–40

Contents lists available at ScienceDirect

Organic Electronics

journal homepage: www.elsevier.com/locate/orgel

Detailed analysis and contact properties of low-voltage organic thin-film transistors based on dinaphtho[2,3-*b*:2′,3′-*f*]thieno[3,2-*b*] thiophene (DNTT) and its didecyl and diphenyl derivatives

Ulrike Kraft [a, b, *], Kazuo Takimiya [c], Myeong Jin Kang [d], Reinhold Rödel [a], Florian Letzkus [e], Joachim N. Burghartz [e], Edwin Weber [b], Hagen Klauk [a]

[a] Max Planck Institute for Solid State Research, Stuttgart, Germany
[b] Department of Chemistry, Technical University Bergakademie Freiberg, Germany
[c] Emergent Molecular Function Research Group, RIKEN Center for Emergent Matter Science (CEMS), Wako, Saitama, Japan
[d] Department of Applied Chemistry, Hiroshima University, Higashi-Hiroshima, Japan
[e] Institute for Microelectronics/IMS Chips, Stuttgart, Germany

ARTICLE INFO

Article history:
Received 19 February 2016
Received in revised form
18 April 2016
Accepted 23 April 2016

Keywords:
Organic field-effect transistors
Contact resistance
Organic semiconductors
Thin-film morphology
Dinaphthothienothiophene (DNTT)

ABSTRACT

Low-voltage organic thin-film transistors (TFTs) based on four different small-molecule semiconductors (pentacene, DNTT (dinaphtho[2,3-b:2′,3′-f]thieno[3,2-*b*]thiophene), C_{10}-DNTT and DPh-DNTT) were fabricated, and a detailed comparison of the semiconductor thin-film morphology, of the current-voltage characteristics of transistors with channel lengths ranging from 100 to 1 μm, and of the contact resistances is provided. The three thienoacene derivatives DNTT, C_{10}-DNTT and DPh-DNTT all have significantly larger charge-carrier mobilities and smaller contact resistances than pentacene. In terms of the intrinsic channel mobility (determined using the transmission line method), C_{10}-DNTT and DPh-DNTT perform quite similarly and notably better than DNTT, suggesting that the decyl substituents in C_{10}-DNTT and the phenyl substituents in DPh-DNTT provide a similar level of enhancement of the charge-transport characteristics over DNTT. However, the DPh-DNTT TFTs have a substantially smaller contact resistance than both the DNTT and the C_{10}-DNTT TFTs, resulting in notably larger effective mobilities, especially in transistors with very small channel lengths. For DPh-DNTT TFTs with a channel length of 1 μm, an effective mobility of 0.68 cm^2/V was determined, together with an on/off ratio of 10^8 and a subthreshold swing of 100 mV/decade.

1. Introduction

For two decades, pentacene has been the most popular small-molecule semiconductor for the fabrication of organic thin-film transistors (TFTs), due mainly to its large field-effect mobility and the ease with which it can be synthesized, purified and processed [1–3]. The dominance of pentacene in organic TFTs is, however, being challenged by several candidate materials from the family of small-molecule thienoacenes [4,5]. In particular, the six-ring compound dinaphtho[2,3-*b*:2′,3′-*f*]thieno[3,2-*b*]thiophene (DNTT [6]) and its alkyl and phenyl derivatives 2,9-didecyl-DNTT (C_{10}-DNTT [7,8]) and 2,9-diphenyl-DNTT (DPh-DNNT [7,9]) have recently demonstrated carrier mobilities rivaling those of pentacene while providing notably better stability [10–12].

Carrier mobilities reported for DNTT TFTs are typically between 2 and 3 cm^2/Vs [6,11,13–17], with a few reports of mobilities around 5 cm^2/Vs for TFTs with large single crystal-like domains [18] and around 9 cm^2/Vs in DNTT single-crystals [19,20]. For C_{10}-DNTT, mobilities can be as large as 8 cm^2/Vs in polycrystalline films [8,21,22] and as large as 12 cm^2/Vs in single-crystals [23]. The observation that C_{10}-DNTT often provides larger carrier mobilities than DNTT [8] has been theoretically rationalized by Northrup et al., who confirmed that the attractive van der Waals interactions between the decyl substituents of neighboring C_{10}-DNTT molecules lead to a tighter molecular packing and hence to a greater orbital overlap compared with DNTT [24]. This is in line with the red shift observed in the thin-film optical absorption spectra of alkyl-DNTT derivatives [8] and with earlier observations of a similar effect in

* Corresponding author. Max Planck Institute for Solid State Research, Stuttgart, Germany
E-mail address: ukraft@stanford.edu (U. Kraft).

http://dx.doi.org/10.1016/j.orgel.2016.04.038
1566-1199/

decyl-substituted tetrathiafulvalene derivatives [25], and it also explains the large carrier mobilities in alkylated benzothieno[3,2-*b*] benzothiophene derivatives [26–29].

For DPh-DNTT, only a few publications exist, with reported carrier mobilities ranging from 2 to 4 cm^2/Vs [7,9,12,17]. The observation that the mobilities reported for DPh-DNTT are smaller than those reported for C_{10}-DNTT is consistent with the above-mentioned explanation regarding the beneficial effect of the long alkyl substituents of C_{10}-DNTT, which are absent in DPh-DNTT. However, closer inspection of the previous publications reveals that the large mobilities (~8 cm^2/Vs) reported for C_{10}-DNTT were obtained exclusively in devices fabricated on atomically smooth surfaces (doped silicon serving as the substrate and gate electrode, with thermally grown SiO_2 as the gate dielectric) and operated with voltages of 40 V or more [8,21,22]. In contrast, when C_{10}-DNTT TFTs are fabricated in a more practical device structure that includes metallic bottom gate electrodes (which necessarily introduce a certain degree of surface roughness) and a gate dielectric that allows the TFTs to be operated with usefully low voltages, the carrier mobilities tend to be smaller, around 4 cm^2/Vs [30–32], which is similar to those reported for DPh-DNTT [7,9,12,17]. Therefore, it appears that the carrier mobility in C_{10}-DNTT is more sensitive to the specifics of the device architecture than the mobility in DNTT and DPh-DNTT, which makes it difficult to rank these three semiconductors in terms of their achievable performance across different TFT architectures.

Therefore, we provide here a comparison of the electrical characteristics of low-voltage pentacene, DNTT, C_{10}-DNTT and DPh-DNTT TFTs, all fabricated using the same device structure that includes metallic bottom gate electrodes and a thin, low-temperature-processed gate dielectric compatible with flexible plastic substrates. A schematic cross-section of the TFTs and the chemical structures of the four organic semiconductors are shown in Fig. 1.

It was found that all three thienoacenes indeed provide carrier mobilities significantly larger than that of pentacene. Surprisingly, the effective field-effect mobility of the DPh-DNTT TFTs (5.9 cm^2/Vs) was found to be larger than that of the C_{10}-DNTT TFTs (5.3 cm^2/Vs). However, we also found that this performance advantage of DPh-DNTT over C_{10}-DNTT (at least in the device configuration employed in our study) is not due to a larger intrinsic channel mobility (which was found to be identical for both semiconductors), but to a significantly smaller contact resistance (0.24 kΩcm for DPh-DNTT *vs.* 0.49 kΩcm for C_{10}-DNTT).

2. Experimental

All TFTs were fabricated on heavily doped silicon substrates in the inverted staggered (bottom-gate, top-contact) device structure (see Fig. 1). A 30 nm thick layer of aluminum was deposited as a common gate electrode by thermal evaporation in vacuum. The aluminum surface was briefly exposed to an oxygen plasma in order to increase the thickness of the native aluminum oxide to about 3.6 nm. The substrates were then immersed into a 2-propanol solution of *n*-tetradecylphosphonic acid (PCI Synthesis, Newburyport, MA, U.S.A.) to allow a densely packed molecular self-assembled monolayer (SAM) with a thickness of about 1.7 nm to self-assemble on the aluminum oxide surface [10–14]. This results in an AlO_x/SAM gate dielectric with a thickness of about 5.3 nm that enables low-voltage operation and is fully compatible with large-area plastic substrates [17].

Subsequently, a nominally 25 nm thick layer of the organic semiconductor was deposited by thermal sublimation in vacuum, with the substrate held at a temperature of 60 °C (for pentacene and DNTT) or 80 °C (for C_{10}-DNTT and DPh-DNTT). The nominal film thickness (25 nm) was monitored using a quartz microbalance. TFTs were completed by the deposition of 30 nm thick Au source and drain contacts onto the organic semiconductor layer through high-resolution silicon stencil masks, which facilitate the definition of channel lengths as small as 1 μm. All electrical measurements were performed immediately after fabrication in ambient air at room temperature under yellow laboratory light. The capacitance of the AlO_x/SAM gate dielectric was measured on metal-insulator-metal capacitors for frequencies from 10 Hz to 10 kHz (Fig. S8).

3. Results and discussion

3.1. Semiconductor thin-film morphology

The morphology of the vacuum-deposited semiconductor films was measured by scanning electron microscopy (SEM). The reason we used SEM is that the topography of the C_{10}-DNTT and DPh-DNTT films is characterized by a large density of nanoscale features that protrude by several hundred nanometers from the surface of the films, making the use of atomic force microscopy (AFM) for these two semiconductors problematic [17]. The SEM images for all four semiconductors (pentacene, DNTT, C_{10}-DNTT and DPh-DNTT) are shown in Fig. 2. In addition, AFM images of pentacene and DNTT films are shown in Figs. S1 and S2.

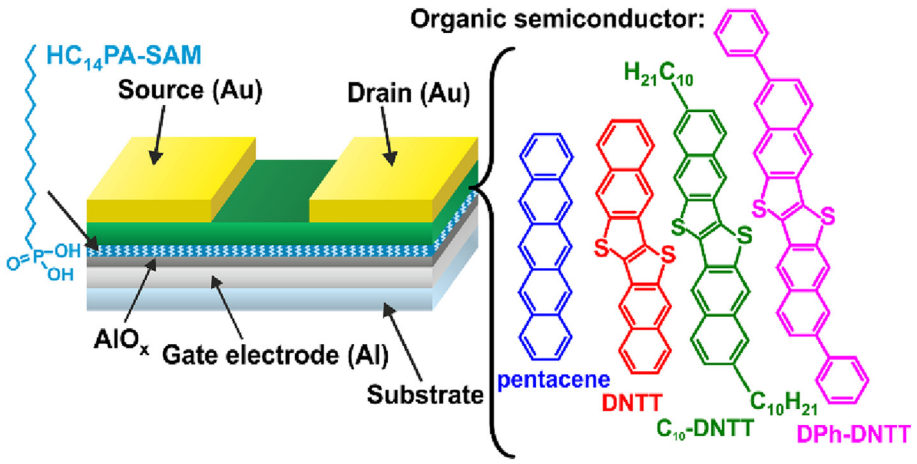

Fig. 1. Schematic cross-section of the thin-film transistors, and chemical structures of the four organic semiconductors investigated in this study (pentacene, DNTT, C_{10}-DNTT and DPh-DNTT).

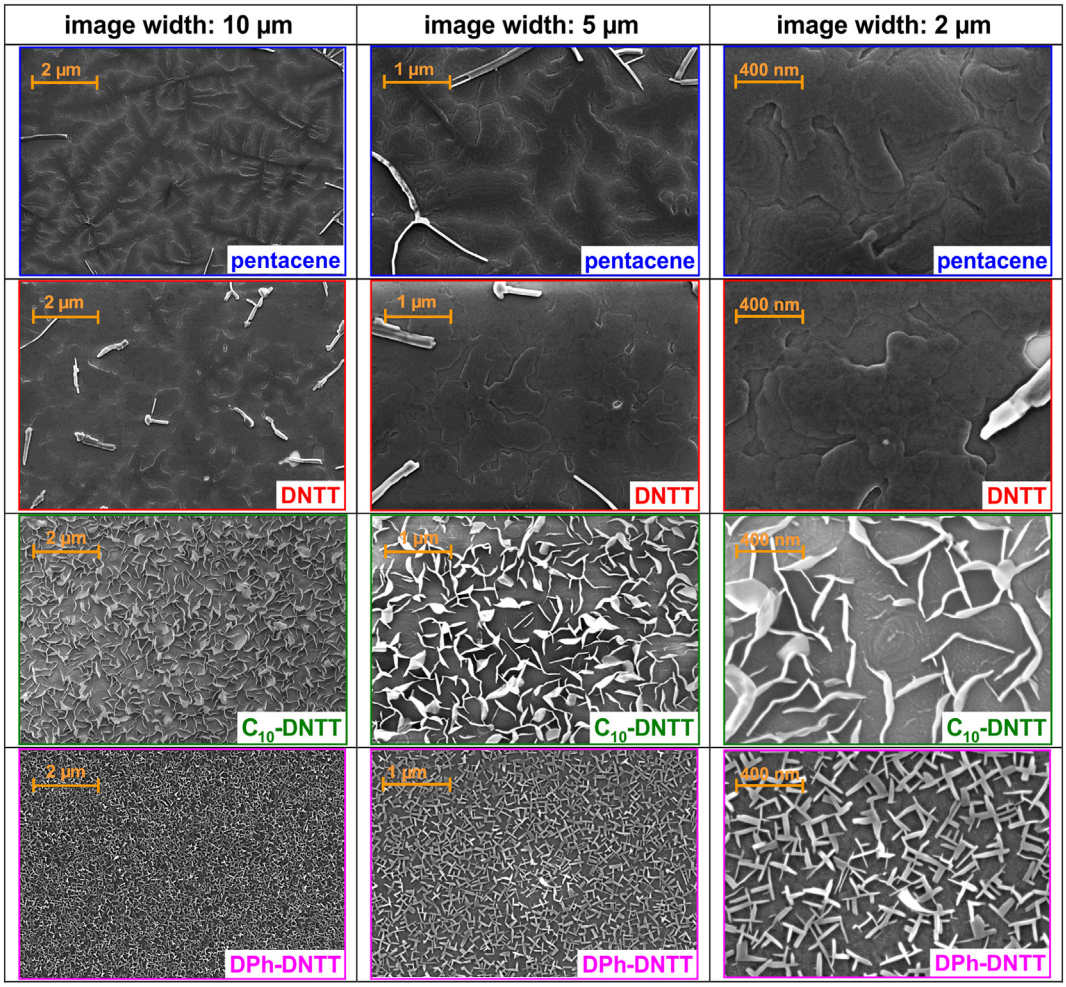

Fig. 2. Thin-film morphology of the vacuum-deposited organic semiconductors. The images were obtained by scanning electron microscopy (SEM) with an acceleration voltage of 1.0–1.5 kV. Image width (from left to right): 10 µm, 5 µm, 2 µm.

The pentacene films show the familiar morphology characterized by large dendritic, terraced grains composed of the well-documented thin-film phase of pentacene [33]. In contrast, the branched, rod-shaped nanoscale features scattered across the surface are possibly composed of the pentacene bulk phase [33–35].

The DNTT films are also characterized by large dendritic and terraced grains, and rod-shaped nanoscale features can also be seen on the surface, although they appear to have a smaller aspect ratio compared with the longer, thinner pentacene features.

Large, terraced grains can also be seen in the C_{10}-DNTT films, although the shape of these grains appears round or elliptic, rather than dendritic. The most striking feature of the C_{10}-DNTT films is the large density of tall, thin, curved lamellae that protrude by several hundred nanometers from the surface. The crystal structure of these lamellae was previously analyzed by x-ray diffraction [21].

The DPh-DNTT films are composed of large terraced grains characterized by relatively straight edges and sharp corners. Nanoscale features can again be seen to protrude from the surface, but with a density that is even greater than in the case of the C_{10}-DNTT films and with a shorter, more compact and less curved geometry and a nearly square-shaped cross-section (see also Fig. S3).

The formation of the large density of crystalline nanoscale features in the C_{10}-DNTT and DPh-DNTT films is possibly related to the significant van der Waals forces between the alkyl chains of neighboring molecules in the case of C_{10}-DNTT [5,21] and by the enhanced π-π interactions in the case of DPh-DNTT. The extent to which these crystalline nanoscale features contribute to the charge transport is unknown, but since they do not appear to form a connected network, it is unlikely that they sustain lateral charge transport over macroscopic distances [21].

3.2. Long-channel thin-film transistors

TFTs based on all four semiconductors were fabricated on heavily doped silicon substrates with an Al gate electrode, a thin AlO_x/SAM gate dielectric, a 25 nm thick semiconductor layer and Au source/drain contacts patterned using a silicon stencil mask [13,17,36]. All electrical measurements were performed in ambient air at room temperature. Fig. 3 shows the measured transfer and output characteristics of a pentacene, a DNTT, a C_{10}-DNTT and a DPh-DNTT TFT, all having a channel length (L) of 100 µm and a channel width (W) of 200 µm (see also Fig. S4).

Owing to the small thickness (5.3 nm) and large capacitance (700 nF/cm^2; see Fig. S8) of the AlO_x/SAM gate dielectric, the TFTs can be operated with relatively low voltages of 3 V [37,38]. Regardless of the semiconductor, the transfer characteristics of all TFTs display a small negative threshold voltage (−0.67 to −1.4 V), a large on/off current ratio (10^6 to 10^7), and a steep subthreshold swing (81–140 mV/decade). Depending on the choice of the semiconductor, the carrier mobility of these long-channel TFTs

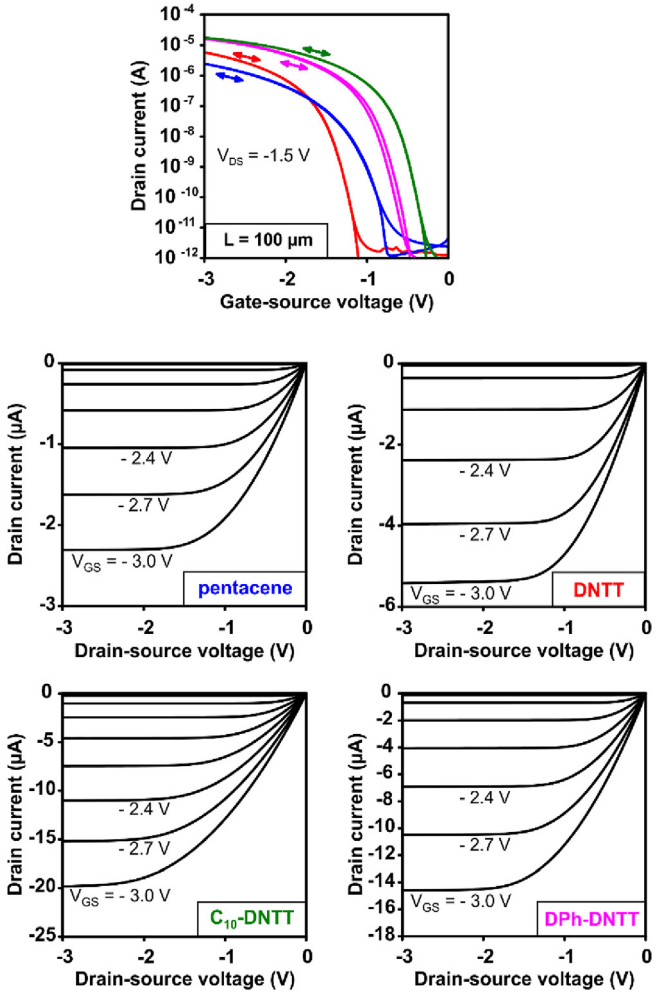

Fig. 3. Measured transfer and output characteristics of TFTs based on pentacene (blue), DNTT (red), C_{10}-DNTT (green) and DPh-DNTT (purple), all having a channel length of 100 µm and a channel width of 200 µm. (For interpretation of the references to color in this figure legend, the reader is referred to the web version of this article.)

(L = 100 µm) ranges from 1.2 cm^2/Vs for pentacene to 3.7 cm^2/Vs for DNTT, 5.3 cm^2/Vs for C_{10}-DNTT and 5.9 cm^2/Vs for DPh-DNTT. The carrier mobilities obtained for DNTT, C_{10}-DNTT, and DPh-DNTT are the highest mobilities reported for low-voltage (<20 V) thin-film transistors based on these three semiconductors.

The observation that the carrier mobility in DPh-DNTT is larger than that in DNTT may be surprising, since quantum-mechanical calculations suggest that the intermolecular transfer integrals in DPh-DNTT are smaller than those in DNTT [5,9]. However, these calculations also show that charge transport in DPh-DNTT is more isotropic than in DNTT [4], which has to be considered as a crucial advantage in terms of the charge-carrier mobility, especially in polycrystalline thin-film transistors.

The good reproducibility of the performance parameters of these TFTs is illustrated in Fig. 4, which shows the measured transfer characteristics of 44 TFTs fabricated on 30 different substrates over a period of three years, i.e. different batches of the organic semiconductors and the contact metals were utilized. The average carrier mobilities, threshold voltages and subthreshold swings are listed in Table 1 (see also Fig. S5) As can be seen, the carrier mobilities vary by about 5% for the DPh-DNTT TFTs, by about 10% for the DNTT and C_{10}-DNTT TFTs and by about 17% for the pentacene TFTs. The threshold voltages vary by less than 0.1 V, and

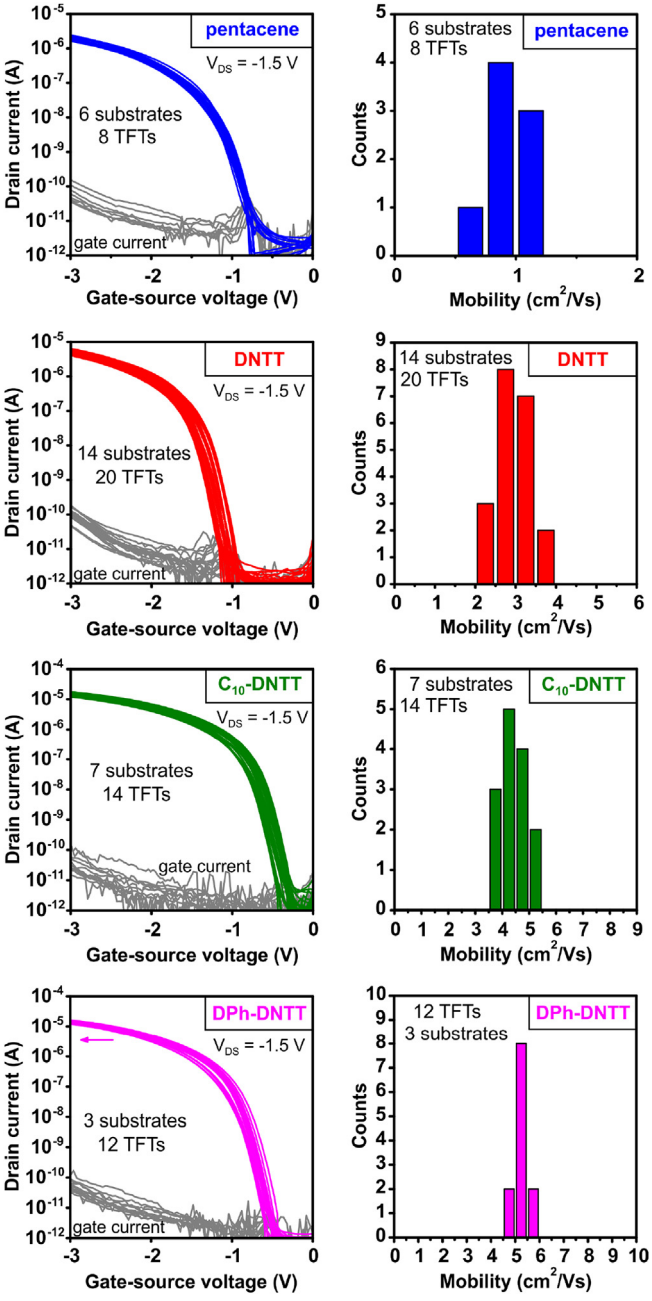

Fig. 4. Measured transfer characteristics of 44 TFTs fabricated on 30 different substrates over a period of three years, showing the good reproducibility of the device parameters. All TFTs have a channel length of 100 µm and a channel with of 200 µm.

the subthreshold swings vary by about 6 mV/decade.

3.3. Short-channel thin-film transistors

For integration of TFTs into high-resolution active-matrix displays [39] or fast integrated circuits [40], a high cut-off frequency $f_T = g_m/(2\pi C_G)$ and hence a large transconductance g_m and a small gate capacitance C_G are often desirable. Both can be achieved by defining a small channel length, since $g_m \sim L^{-1}$ and $C_G \sim L$ [13,41].

Fig. 5 shows the measured transfer and output characteristics of a pentacene, a DNTT, a C_{10}-DNTT and a DPh-DNTT TFT, all having a channel length of 1 µm and a channel width of 200 µm (see also Fig. S6). The DPh-DNTT TFT has an on/off ratio of 10^8 and a

Table 1
Average effective field-effect mobility, threshold voltage and subthreshold swing of 44 TFTs fabricated on 30 different substrates over a period of three years (see also Fig. 4). All TFTs have a channel length of 100 μm and a channel width of 200 μm.

Semiconductor	Number of TFTs	Number of substrates	Average effective field-effect mobility (cm^2/Vs)	Average threshold voltage (V)	Average subthreshold swing (mV/decade)
Pentacene	8	6	0.99 ± 0.17	−1.22 ± 0.07	132 ± 6
DNTT	20	14	2.96 ± 0.39	−1.37 ± 0.08	87 ± 4
C_{10}-DNTT	14	7	4.43 ± 0.47	−0.67 ± 0.09	89 ± 6
DPh-DNTT	12	3	5.29 ± 0.30	−0.93 ± 0.09	87 ± 4

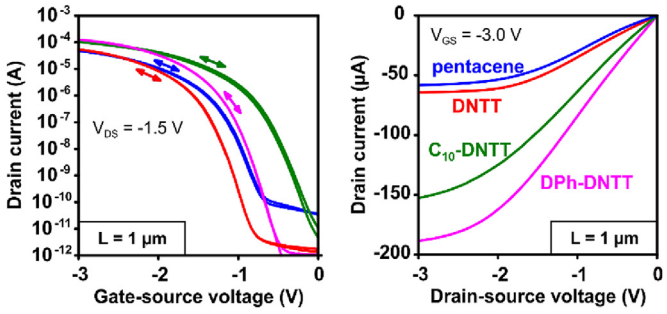

Fig. 5. Measured transfer and output characteristics of TFTs based on pentacene (blue), DNTT (red), C_{10}-DNTT (green) and DPh-DNTT (purple), all having a channel length of 1 μm and a channel width of 200 μm. (For interpretation of the references to color in this figure legend, the reader is referred to the web version of this article.)

subthreshold swing of 100 mV/decade, which is the steepest subthreshold swing reported for an organic TFT with such a small channel length. The channel-width-normalized transconductance (0.51 S/m) is about an order of magnitude larger than at a channel length of 100 μm, which confirms the beneficial effect of a small channel length. However, based on the theoretical relationship between the transconductance and the channel length ($g_m \sim L^{-1}$) [17], an even greater improvement of two orders of magnitude was to be expected. The reason for the smaller-than-expected improvement in the transconductance upon reducing the channel length is that a smaller channel length also leads to a greater relative contribution of the contact resistance to the total device resistance, so that the effective field-effect mobility μ_{eff} can drop significantly below the intrinsic channel mobility μ_0, and this will also affect the transconductance, since $g_m \sim \mu_{eff}$ [17]. In the case of our DPh-DNTT TFTs, the effective mobility is still 2.7 cm^2/Vs at a channel length of 10 μm, but only 0.68 cm^2/Vs at a channel length of 1 μm (see also Table 2 and Table S1 for the linear regime).

For a more quantitative analysis, the effective field-effect mobility extracted from the transfer characteristics of TFTs in the linear regime ($V_{DS} = -0.1$ V) based on all four semiconductors is plotted in Fig. 6a as a function of the channel length, which we have varied from 100 μm to 1 μm for this analysis. The intrinsic channel mobility (μ_0) and the channel length at which the contact resistance is equal to the channel resistance ($L_{1/2}$) can be obtained by fitting the measurement data (μ_{eff} *vs.* L) to the following equation [42,43]:

$$\mu_{eff} = \frac{\mu_0}{1 + \frac{L_{1/2}}{L}} \quad (1)$$

For the data in Fig. 6a, intrinsic channel mobilities of 1.5 cm^2/Vs for pentacene, 3.7 cm^2/Vs for DNTT, 5.6 cm^2/Vs for C_{10}-DNTT and 5.9 cm^2/Vs for DPh-DNTT are obtained using Equation (1) (see also Table 3). The channel length at which the contact resistance is equal to the channel resistance ($L_{1/2}$) ranges from 14 μm (DNTT and DPh-DNTT) to 19 μm (pentacene) and 27 μm (C_{10}-DNTT).

3.4. Contact resistance

To determine the contact resistance of the TFTs, we applied the transmission line method (TLM) [13,17,43–48]. In this approach, the total resistance of the transistors is modeled as the sum of the contact resistance and the channel resistance. When the channel-width-normalized total resistance $R_{total} \cdot W$ in the linear regime is plotted as a function of the channel length, the width-normalized contact resistance $R_C \cdot W$ can be extracted by extrapolating the linear fit to the data to a channel length of zero, where the channel resistance $R_{channel}$ disappears, and the intrinsic channel mobility μ_0 can be obtained from the slope of the linear fit [13,43,44,46,47]:

$$R_{total} = R_C + R_{channel}$$

$$R_{total}W = R_C W + \frac{L}{\mu_0 C_{diel}(V_{GS} - V_{th})} \quad \text{(linear regime)} \quad (2)$$

with

Table 2
Effective field-effect mobility, threshold voltage, subthreshold swing, transconductance and on/off current ratio of pentacene, DNTT, C_{10}-DNTT and DPh-DNTT TFTs with three representative channel lengths (100 μm, 10 μm, 1 μm; channel width: 200 μm) in the saturation regime ($V_{DS} = -1.5$ V).

Semiconductor	Channel length (μm)	Effective field-effect mobility (cm^2/Vs)	Threshold Voltage (V)	Subthreshold swing (mV/decade)	Transconductance (S/m)	On/off current ratio
Pentacene	100	1.2	−1.28	138	0.013	10^6
	10	0.6	−1.29	112	0.061	10^7
	1	0.24	−1.19	130	0.21	10^6
DNTT	100	3.7	−1.47	86	0.035	10^7
	10	1.6	−1.38	84	0.14	10^7
	1	0.34	−1.41	104	0.26	10^7
C_{10}-DNTT	100	5.3	−0.62	81	0.054	10^7
	10	2.1	−0.64	102	0.2	10^8
	1	0.38	−0.73	121	0.31	10^8
DPh-DNTT	100	5.9	−0.88	84	0.06	10^7
	10	2.7	−1.19	94	0.28	10^8
	1	0.68	−1.17	101	0.51	10^8

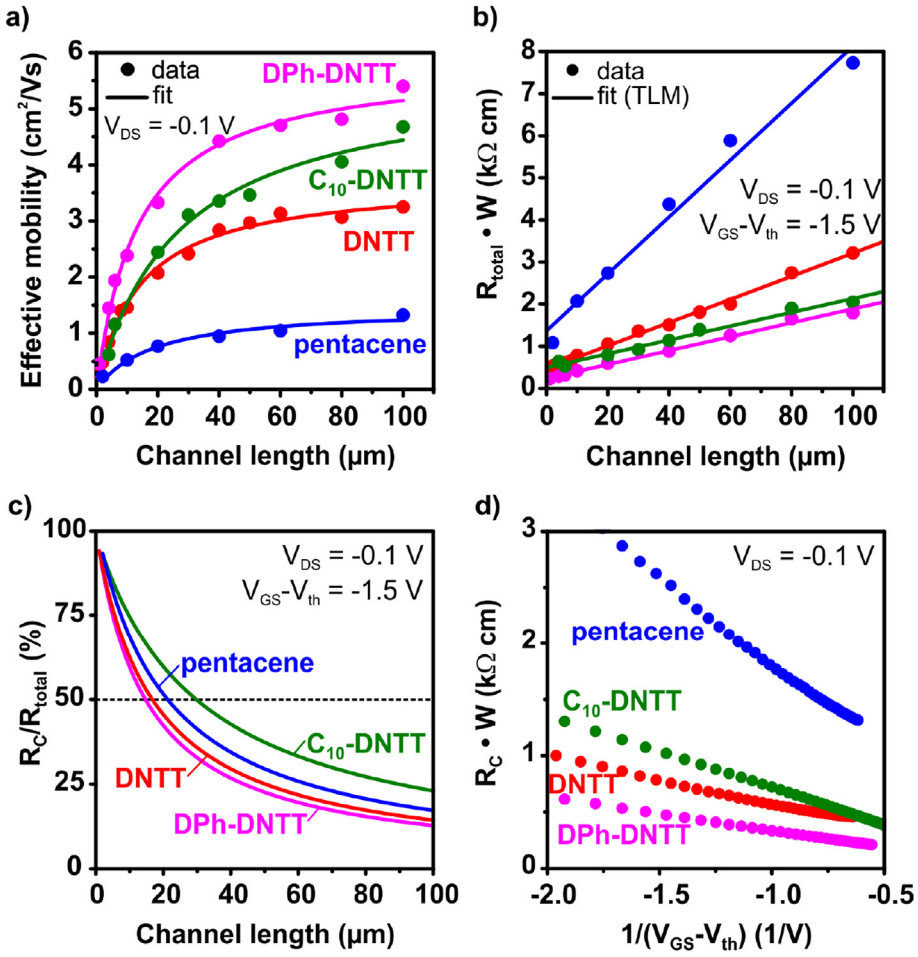

Fig. 6. a) Effective field-effect mobility in the linear regime ($V_{DS} = -0.1$ V) as a function of the channel length. Fitting the data to Equation (1) yields the intrinsic channel mobility (μ_0) and the channel length at which the contact resistance is equal to the channel resistance ($L_{1/2}$; see Tables 3 and 4). b) Channel-width-normalized total resistance ($R_{total} \cdot W$) in the linear regime ($V_{DS} = -0.1$ V; $V_{GS} - V_{th} = -1.5$ V) as a function of the channel length. Fitting the data to Equation (2) yields the intrinsic channel mobility (μ_0) and the channel-width-normalized contact resistance ($R_C \cdot W$; see Table 3). c) Ratio between the contact resistance and the total resistance in the linear regime as a function of the channel length. The data were obtained from the linear fits in Fig. 6b. From these data, the channel length at which the contact resistance is equal to the channel resistance ($L_{1/2}$) can be extracted (see Table 4). d) Channel-width-normalized contact resistance ($R_C \cdot W$) in the linear regime ($V_{DS} = -0.1$ V) as a function of the inverse gate overdrive voltage ($1/(V_{GS} - V_{th})$).

Table 3
Intrinsic channel mobility, width-normalized contact resistance, transfer length and sheet resistance of pentacene, DNTT, C_{10}-DNTT and DPh-DNTT TFTs extracted with the transmission line method (Equation (2)) in the linear regime ($V_{DS} = -0.1$ V; $V_{GS} - V_{th} = -1.5$ V; see Fig. 6). The intrinsic channel mobility calculated using Equation (1) is shown for comparison.

Semiconductor	Intrinsic channel mobility μ_0 from Eq. (1) (cm^2/Vs)	Intrinsic channel mobility μ_0 from Eq. (2) (cm^2/Vs)	Width-normalized contact resistance $R_C \cdot W$ (kΩcm)	Transfer length L_T (μm)	Sheet resistance R_{sheet} (kΩ/sq)
Pentacene	1.5 ± 0.1	1.4 ± 0.1	1.4 ± 0.3	10.1 ± 2.0	676 ± 49
DNTT	3.7 ± 0.1	3.5 ± 0.1	0.46 ± 0.02	8.4 ± 0.4	275 ± 5
C_{10}-DNTT	5.6 ± 0.3	5.7 ± 0.3	0.49 ± 0.05	15.1 ± 2.0	164 ± 9
DPh-DNTT	5.9 ± 0.2	5.7 ± 0.2	0.24 ± 0.03	7.2 ± 0.8	165 ± 5

Table 4
Channel length at which the contact resistance is equal to the channel resistance ($L_{1/2}$). The values in the left column were obtained by fitting the data in Fig. 6a to Equation (1), while the values in the right column were extracted from Fig. 6c.

Semiconductor	$L_{1/2}$ from Eq. (1) (μm)	$L_{1/2}$ from Eq. (2) (μm)
Pentacene	19 ± 5	~21
DNTT	14 ± 0.1	~17
C_{10}-DNTT	27 ± 4	~30
DPh-DNTT	14 ± 1.3	~15

$$R_{sheet} = \frac{R_{channel} \cdot W}{L} = \frac{1}{\mu_0 \cdot C_{diel} \cdot (V_{GS} - V_{th})}$$

where C_{diel} is the gate-dielectric capacitance per unit area (700 nF/cm^2) and R_{sheet} is the sheet resistance. In order to account for the differences between the threshold voltages of the various TFTs, only resistance data measured at a fixed gate overdrive voltage (*i.e.*, at a fixed gate-source voltage above threshold; $V_{GS} - V_{th}$) were used for the TLM analysis; this assures that only contact resistances obtained at the same bias condition are compared.

Fig. 6b shows the channel-width-normalized total resistance

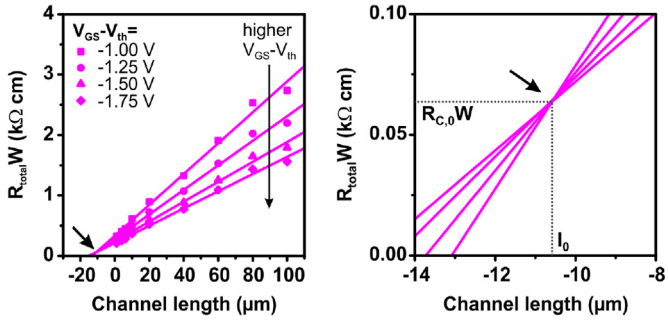

Fig. 7. Width-normalized total resistance of DPh-DNTT TFTs as a function of the channel length for four different gate overdrive voltages determined using TLM. All linear fit curves meet at a single point which defines a characteristic length l_0 = 10.5 μm and a characteristic width-normalized resistance $R_{C,0}\cdot W$ = 0.065 kΩcm.

($R_{total}\cdot W$) of pentacene, DNTT, C_{10}-DNTT and DPh-DNTT TFTs measured at a gate overdrive voltage of −1.5 V as a function of the channel length. From the linear fits to the measured data, channel-width-normalized contact resistances and intrinsic channel mobilities of 1.4 kΩcm and 1.4 cm^2/Vs for pentacene, 0.46 kΩcm and 3.5 cm^2/Vs for DNTT, 0.49 kΩcm and 5.7 cm^2/Vs for C_{10}-DNTT and 0.24 kΩcm and 5.7 cm^2/Vs for DPh-DNTT were obtained (see also Table 3). These values compare favorably with contact resistances reported in literature for derivatives of DNTT and similar thienoacenes [13,17,20,49–51]. Note that the values for the intrinsic channel mobilities obtained by fitting the measurement data to Equations (1) and (2) are almost identical (see also Table 3).

The results show that the intrinsic channel mobilities of C_{10}-DNTT and DPh-DNTT are very similar, but that the contact resistance of the DPh-DNTT TFTs is significantly smaller than that of the DNTT and C_{10}-DNTT TFTs (0.24 kΩcm *vs.* 0.46 and 0.49 kΩcm). These differences in contact resistance can be understood by considering both the differences in the molecular structure and the differences in the thin-film morphology of the three semiconductors: For C_{10}-DNTT, the long aliphatic substituents protruding from the conjugated core of the molecules likely impede the charge transport in the vertical direction and hence the efficient exchange of charges between the molecules and the source and drain contacts located on top of the semiconductor layer, which explains the observation that the C_{10}-DNTT TFTs have the largest contact resistance. To explain the difference in contact resistance between the DNTT TFTs and the DPh-DNTT TFTs, it is helpful to compare the morphologies of the DNTT and DPh-DNTT films (see Fig. 2): While the DNTT films appear quite smooth and even, the DPh-DNTT films are characterized by a large density of distinctly three-dimensional features that lead to a larger effective surface area and to regions in which the actual film thickness is smaller than the nominal (average) film thickness, and both of these effects are expected to lead to a smaller contact resistance compared to the DNTT TFTs.

As a result of the smaller contact resistance, the DPh-DNTT TFTs have the larger effective mobility, especially when the channel length is small: At a channel length of 1 μm, the DPh-DNTT TFTs have an effective mobility of 0.68 cm^2/Vs, compared with 0.38 cm^2/Vs for the C_{10}-DNTT TFTs (see also Table 2).

As mentioned above, the contribution of the contact resistance to the total device resistance increases monotonically with decreasing channel length; see Equation (2) (see also Fig. S7). This can also be seen in Fig. 6c where the ratio between the contact resistance and the total resistance is plotted as a function of the channel length for all four semiconductors. From this data, the specific channel length ($L_{1/2}$) at which the contact resistance accounts for 50% of the total resistance and hence equals the channel resistance can be extracted. As expected, the values for $L_{1/2}$ obtained in this manner are very similar to the values obtained by fitting the data in Fig. 6a to Equation (1) (see Table 4). Since $L_{1/2}$ is the ratio between the width-normalized contact resistance and the channel sheet resistance ($L_{1/2} = R_C\cdot W/R_{sheet}$), $L_{1/2}$ of TFTs that have similar contact resistance (such as DNTT and C_{10}-DNTT) scales approximately linearly with the channel sheet conductance, and hence with the intrinsic channel mobility [22].

The values obtained for $L_{1/2}$, which are summarized in Table 4, indicate that TFTs based on DNTT and DPh-DNTT are less severely affected by an aggressive reduction of the channel length than TFTs based on pentacene and C_{10}-DNTT, which is an important consideration in view of high-frequency TFTs for display and circuit applications [39,40].

By performing TLM measurements over a range of gate-source voltages ($V_{GS} \approx -0.5$ V to −2 V), the dependence of the contact resistance on the gate-source voltage (or on the gate overdrive voltage, $V_{GS} - V_{th}$) can be analyzed. As can be seen in Fig. 6d, the contact resistance of TFTs based on all four semiconductors shows an approximately linear increase with the inverse of the gate overdrive voltage ($R_C\cdot W \propto 1/(V_{GS} - V_{th})$) [44,46,52], which is in agreement with the current crowding model. However, the slope of this relationship is different for the four semiconductors, *i.e.*, the degree to which the contact resistance is modulated by the applied gate-source voltage is smallest for DNTT and largest for pentacene. According to an empirical model that was proposed by Luan et al. [53] for bottom-gate, top-contact TFTs based on hydrogenated amorphous silicon, the width-normalized contact resistance $R_C\cdot W$ is composed of a constant part ($R_{C,0}\cdot W$) and a gate-source-voltage-dependent part and can be expressed as [47,53,54]:

$$R_C\cdot W = R_{C,0}\cdot W + \frac{l_0}{\mu_C C_{diel}(V_{GS} - V_{th})} \quad (3)$$

Fig. 7 shows the linear TLM fits for DPh-DNTT TFTs for four different gate overdrive voltages ($V_{GS} - V_{th}$). The linear fits all merge at a single point ($-l_0$; $R_{C,0}\cdot W$) from which the gate-source-voltage-independent part of the width-normalized contact resistance (the minimal effective width-normalized contact resistance [53,54]) can be extracted ($y = R_{C,0}\cdot W$). The V_{GS}-dependent part of the contact resistance can be interpreted as an accumulation channel below the source and drain contacts with an effectively extended channel length l_0 and an associated mobility μ_C in the contact region [54]. Like the total contact resistance, the constant part of the contact resistance is smaller for smaller sheet resistances (larger μ_0/larger μ_C). The values extracted for $R_{C,0}\cdot W$, l_0

Table 5
Characteristic parameters l_0 and $R_{C,0}\cdot W$ determined graphically and μ_C determined by a linear fit to Fig. 6d for pentacene, DNTT, C_{10}-DNTT and DPh-DNTT.

Semiconductor	Intrinsic channel mobility μ_0 from Eq. (2) (cm^2/Vs)	Width-normalized contact resistance $R_C\cdot W$ @ $V_{GS} - V_{th} = -1.5$ V (kΩcm)	$R_{C,0}\cdot W$ (kΩcm)	l_0 (μm)	μ_C (cm^2/Vs) from a Fit to Fig. 6d
Pentacene	1.4	1.4	0.6	11.5	1.1
DNTT	3.5	0.46	0.25	7.5	2.6
C_{10}-DNTT	5.7	0.49	0.06	26.5	5.8
DPh-DNTT	5.7	0.24	0.065	10.5	5.2

and μ_C for all four organic semiconductors are summarized in Table 5.

4. Conclusions

In summary, we provide the first comprehensive comparison of low-voltage organic thin-film transistors based on the four small-molecule semiconductors pentacene, DNTT, C_{10}-DNTT and DPh-DNTT. The latter three were all found to provide significantly larger carrier mobilities (up to 5.9 cm^2/Vs in the case of DPh-DNTT) and smaller contact resistances than pentacene. In terms of the intrinsic channel mobility, C_{10}-DNTT and DPh-DNTT were found to perform quite similarly and notably better than DNTT, suggesting that the decyl substituents in C_{10}-DNTT and the phenyl substituents in DPh-DNTT provide a similar level of enhancement of the charge-transport characteristics over DNTT, at least for the particular device architecture investigated in this study. However, DPh-DNTT was found to provide a smaller contact resistance (0.24 kΩcm) than C_{10}-DNTT (0.49 kΩcm), which results in notably larger effective mobilities, especially in transistors with aggressively reduced channel lengths. For a DPh-DNTT TFT with a channel length of 1 μm, an on/off ratio of 10^8, a subthreshold swing of 100 mV/decade, and an effective mobility of 0.68 cm^2/Vs were measured.

Acknowledgements

U.K. gratefully acknowledges expert technical assistance from Bernhard Fenk (Max Planck Institute for Solid State Research) for assistance with scanning electron microscopy. This work was partially funded by the German Research Foundation under Grants KL 2223/5-1 and KL 2223/5-2.

Appendix A. Supplementary data

Supplementary data related to this article can be found at http://dx.doi.org/10.1016/j.orgel.2016.04.038.

References

[1] Y.-Y. Lin, D. Gundlach, S. Nelson, T. Jackson, IEEE Electr. Dev. Lett. 18 (1997) 606.
[2] T.W. Kelley, L.D. Boardman, T.D. Dunbar, D.V. Muyres, M.J. Pellerite, T.P. Smith, J. Phys. Chem. B 107 (2003) 5877.
[3] A. Brown, A. Pomp, C. Hart, D. De Leeuw, Science 270 (1995) 972.
[4] K. Takimiya, S. Shinamura, I. Osaka, E. Miyazaki, Adv. Mater 23 (2011) 4347.
[5] K. Takimiya, I. Osaka, T. Mori, M. Nakano, Acc. Chem. Res. 47 (2014) 1493.
[6] T. Yamamoto, K. Takimiya, J. Am. Chem. Soc. 129 (2007) 2224.
[7] K. Niimi, M.J. Kang, E. Miyazaki, I. Osaka, K. Takimiya, Org. Lett. 13 (2011) 3430.
[8] M.J. Kang, H. Mori, E. Miyazaki, K. Takimiya, M. Ikeda, H. Kuwabara, Adv. Mater 23 (2011) 1222.
[9] M.J. Kang, E. Miyazaki, I. Osaka, K. Takimiya, A. Nakao, ACS Appl. Mater. Interfaces 5 (2013) 2331.
[10] U. Kraft, M. Sejfić, T. Zaki, F. Letzkus, J. Burghartz, K. Takimiya, E. Weber, H. Klauk, 72nd Annual Dev. Res. Conf. Techn. Dig., 2014, http://ieeexplore.ieee.org/xpl/articleDetails.jsp?arnumber=6872407&filter%3DAND%28p_IS_Number%3A6872264%29%26pageNumber%3D6, Accession Number: WOS: 000346309800127; ISBN:978-1-4799-5406-3; ISSN: 1548-3770.
[11] U. Zschieschang, F. Ante, D. Kälblein, T. Yamamoto, K. Takimiya, H. Kuwabara, M. Ikeda, T. Sekitani, T. Someya, J.B. Nimoth, Org. Electron 12 (2011) 1370.
[12] T. Yokota, K. Kuribara, T. Tokuhara, U. Zschieschang, H. Klauk, K. Takimiya, Y. Sadamitsu, M. Hamada, T. Sekitani, T. Someya, Adv. Mater 25 (2013) 3639.
[13] F. Ante, D. Kälblein, T. Zaki, U. Zschieschang, K. Takimiya, M. Ikeda, T. Sekitani, T. Someya, J.N. Burghartz, K. Kern, Small 8 (2012) 73.
[14] K. Fukuda, T. Sekitani, T. Yokota, K. Kuribara, T. Huang, T. Sakurai, U. Zschieschang, H. Klauk, M. Ikeda, H. Kuwabara, IEEE Electr. Dev. Lett. 32 (2011) 1448.
[15] M. Kaltenbrunner, T. Sekitani, J. Reeder, T. Yokota, K. Kuribara, T. Tokuhara, M. Drack, R. Schwödiauer, I. Graz, S. Bauer-Gogonea, Nature 499 (2013) 458.
[16] D.M. Taylor, E.R. Patchett, A. Williams, N.J. Neto, Z. Ding, H.E. Assender, J.J. Morrison, S.G. Yeates, IEEE Trans. Electr. Dev. 61 (2014) 2950.
[17] U. Kraft, M. Sejfić, M.J. Kang, K. Takimiya, T. Zaki, F. Letzkus, J.N. Burghartz, E. Weber, H. Klauk, Adv. Mater 27 (2015) 207.
[18] A. Hamaguchi, T. Negishi, Y. Kimura, Y. Ikeda, K. Takimiya, S.Z. Bisri, Y. Iwasa, T. Shiro, Adv. Mater. 27 (2015) 6606.
[19] S. Haas, Y. Takahashi, K. Takimiya, T. Hasegawa, Appl. Phys. Lett. 95 (2009) 022111.
[20] W. Xie, K. Willa, Y. Wu, R. Häusermann, K. Takimiya, B. Batlogg, C.D. Frisbie, Adv. Mater 25 (2013) 3478.
[21] R. Hofmockel, U. Zschieschang, U. Kraft, R. Rödel, N.H. Hansen, M. Stolte, F. Würthner, K. Takimiya, K. Kern, J. Pflaum, Org. Electron 14 (2013) 3213.
[22] T. Matsumoto, W. Ou-Yang, K. Miyake, T. Uemura, J. Takeya, Org. Electron 14 (2013) 2590.
[23] T. Uemura, K. Nakayama, Y. Hirose, J. Soeda, M. Uno, W. Li, M. Yamagishi, Y. Okada, J. Takeya, Curr. Appl. Phys. 12 (2012) S87.
[24] J.E. Northrup, W. Xie, Y.-Y. Sun, S. Zhang, Appl. Phys. Express 6 (2013) 071601.
[25] H. Inokuchi, G. Saito, P. Wu, K. Seki, T.B. Tang, T. Mori, K. Imaeda, T. Enoki, Y. Higuchi, K. Inaka, Chem. Lett. 15 (1986) 1263.
[26] H. Minemawari, T. Yamada, H. Matsui, J.Y. Tsutsumi, S. Haas, R. Chiba, R. Kumai, T. Hasegawa, Nature 475 (2011) 364.
[27] A.Y. Amin, A. Khassanov, K. Reuter, T. Meyer-Friedrichsen, M. Halik, J. Am. Chem. Soc. 134 (2012) 16548.
[28] Y. Yuan, G. Giri, A.L. Ayzner, A.P. Zoombelt, S.C. Mannsfeld, J. Chen, D. Nordlund, M.F. Toney, J. Huang, Z. Bao, Nat. Commun. 5 (2014) 3005.
[29] G. Nan, Z. Li, J. Mater. Chem. C 2 (2014) 1447.
[30] U. Zschieschang, M.J. Kang, K. Takimiya, T. Sekitani, T. Someya, T.W. Canzler, A. Werner, J. Blochwitz-Nimoth, H. Klauk, J. Mater. Chem. 22 (2012) 4273.
[31] I. Doi, M.J. Kang, K. Takimiya, Curr. Appl. Phys. 12 (2012) e2.
[32] W. Ou-Yang, T. Uemura, K. Miyake, S. Onish, T. Kato, M. Katayama, M. Kang, K. Takimiya, M. Ikeda, H. Kuwabara, M. Hamada, J. Takeya, Appl. Phys. Lett. 101 (2012) 223304–223311.
[33] D. Gundlach, T. Jackson, D. Schlom, S. Nelson, Appl. Phys. Lett. 74 (1999) 3302.
[34] I. Salzmann, S. Duhm, R. Opitz, J.P. Rabe, N. Koch, Appl. Phys. Lett. 91 (2007) 051919.
[35] I. Bouchoms, W. Schoonveld, J. Vrijmoeth, T. Klapwijk, Synth. Met. 104 (1999) 175.
[36] F. Letzkus, J. Butschke, B. Höfflinger, M. Irmscher, C. Reuter, R. Springer, A. Ehrmann, J. Mathuni, Microelectr. Eng. 53 (2000) 609.
[37] H. Klauk, U. Zschieschang, J. Pflaum, M. Halik, Nature 445 (2007) 745. http://www.nature.com/nature/journal/v445/n7129/abs/nature05533.html.
[38] U. Kraft, U. Zschieschang, F. Ante, D. Kälblein, C. Kamella, K. Amsharov, M. Jansen, K. Kern, E. Weber, H. Klauk, J. Mater. Chem. 20 (2010) 6416.
[39] Y. Fujisaki, Y. Nakajima, T. Takei, H. Fukagawa, T. Yamamoto, H. Fujikake, IEEE Trans. Electr. Dev. 59 (2012) 3442.
[40] T. Zaki, F. Ante, U. Zschieschang, J. Butschke, F. Letzkus, H. Richter, H. Klauk, J.N. Burghartz, IEEE J. Solid-State Circ. 47 (2012) 292.
[41] M. Uno, B.-S. Cha, Y. Kanaoka, J. Takeya, Org. Electron 20 (2015) 119.
[42] M. Marinkovic, D. Belaineh, V. Wagner, D. Knipp, Adv. Mater 24 (2012) 4005.
[43] U. Kraft, J.E. Anthony, E. Ripaud, M.A. Loth, E. Weber, H. Klauk, Chem. Mater 27 (2015) 998.
[44] D.K. Schroder, Semiconductor Material and Device Characterization, John Wiley & Sons, 2006.
[45] H. Berger, J. Electrochem. Soc. 119 (1972) 507.
[46] C.-S. Chiang, S. Martin, J. Kanicki, Y. Ugai, T. Yukawa, S. Takeuchi, Jpn. J. Appl. Phys. 37 (1998) 5914.
[47] D. Natali, M. Caironi, Adv. Mater 24 (2012) 1357.
[48] D. Gundlach, L. Zhou, J. Nichols, T. Jackson, P. Necliudov, M. Shur, J. Appl. Phys. 100 (2006) 024509.
[49] T. Uemura, C. Rolin, T.-H. Ke, P. Fesenko, J. Genoe, P. Heremans, J. Takeya, Adv. Mater. 28 (2016) 151.
[50] M. Uno, Y. Kanaoka, B.-S. Cha, N. Isahaya, M. Sakai, H. Matsui, C. Mitsui, T. Okamoto, J. Takeya, T. Kato, M. Katayama, Y. Usami, T. Yamakami, Adv. Electron. Mater. 1 (2015) 1500178.
[51] M. Kitamura, Y. Kuzomoto, Y. Arakawa, Phys. Status Solidi C. 21 (2013) 2586.
[52] T. Richards, H. Sirringhaus, J. Appl. Phys. 102 (2007) 094510.
[53] S. Luan, G.W. Neudeck, J. Appl. Phys. 72 (1992) 766.
[54] J. Zaumseil, K.W. Baldwin, J.A. Rogers, J. Appl. Phys. 93 (2003) 6117.

Supporting Information

Detailed Analysis and Contact Properties of Low-Voltage Organic Thin-Film Transistors based on Dinaphtho[2,3-*b*:2',3'-*f*]thieno[3,2-*b*]thiophene (DNTT) and its Didecyl and Diphenyl Derivatives

Ulrike Kraft, Kazuo Takimiya, Myeong Jin Kang, Reinhold Rödel, Florian Letzkus, Joachim N. Burghartz, Edwin Weber, Hagen Klauk*

1. Organic semiconductor thin-film morphology

Atomic force microscopy (AFM) was conducted using a Nanoscope III Multimode in tapping mode with silicon cantilevers (resonance frequency: 204-497 kHz). The images were processed with WSxM.[S1]

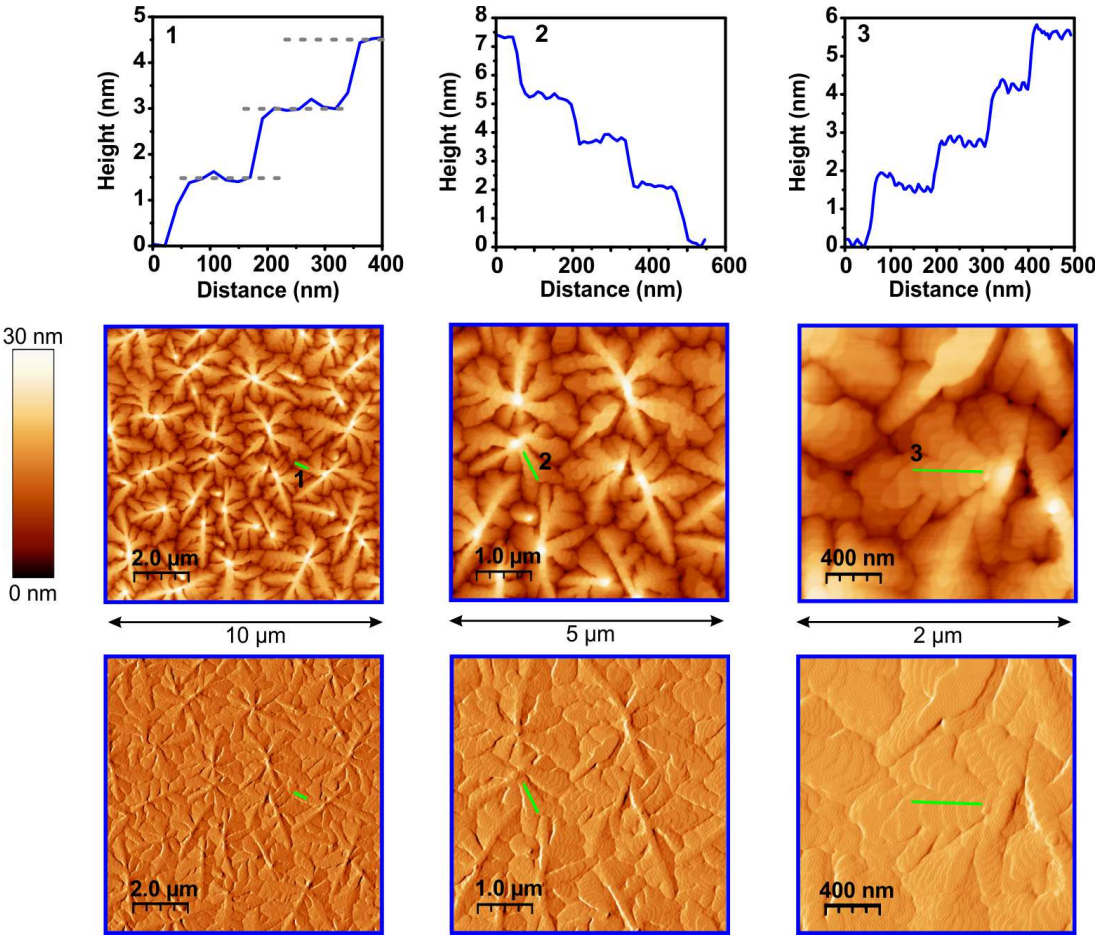

Figure S1. Morphology of a pentacene thin-film (nominal thickness 25 nm) measured by atomic force microscopy (AFM) in tapping mode. Image width (from left to right): 10 µm, 5 µm, 2 µm. For each area size, the topography image (second row), the corresponding height profile (first row) and, the amplitude image (third row) are displayed.

[S1] I. Horcas; R. Fernández; J. M. Gómez-Rodríguez; J. Colchero; J. Gómez-Herrero; A. M. Baro, "WSXM: A software for scanning probe microscopy and a tool for nanotechnology" *Review of Scientific Instruments* **2007**, *78*.

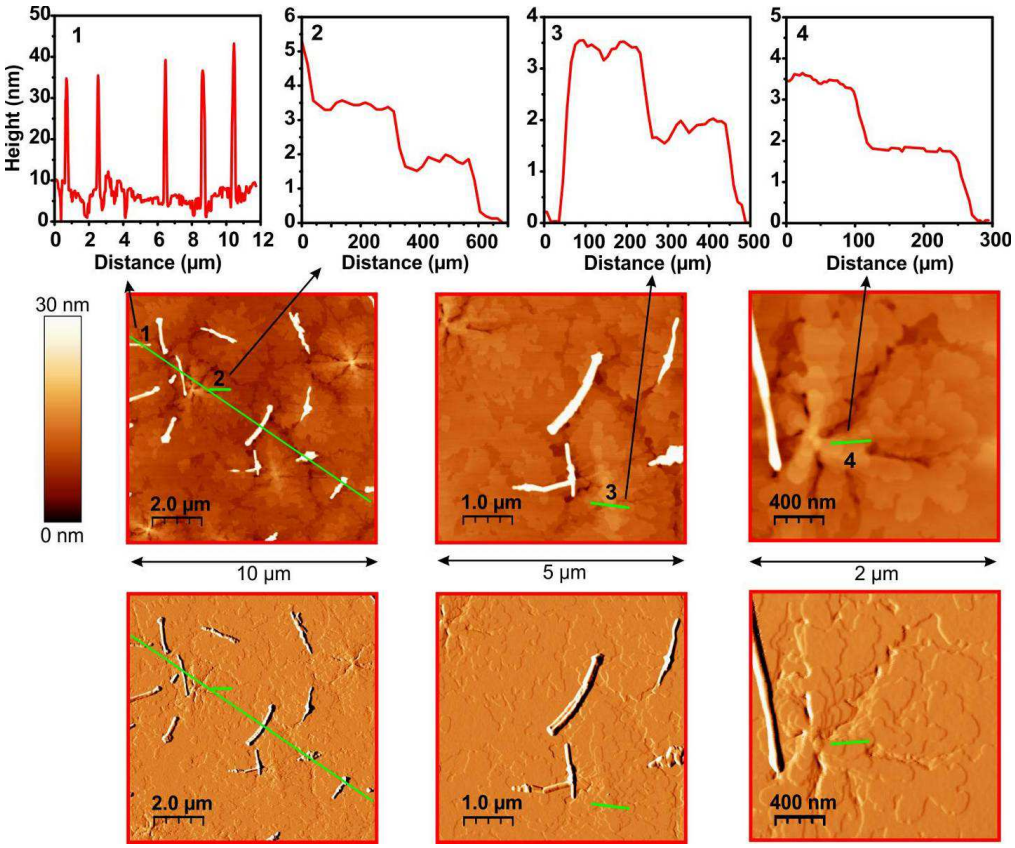

Figure S2. Morphology of a DNTT thin-film (nominal thickness 25 nm) measured by atomic force microscopy (AFM) in tapping mode. Image width (from left to right): 10 µm, 5 µm, 2 µm. For each area size, thetopography image (second row), the corresponding height profile (first row) and, the amplitude image (third row) are displayed. An additional height profile (1) shows that rod-shaped nanoscale features protrude from the surface of the DNTT thin-film by about 30 nm to 40 nm.

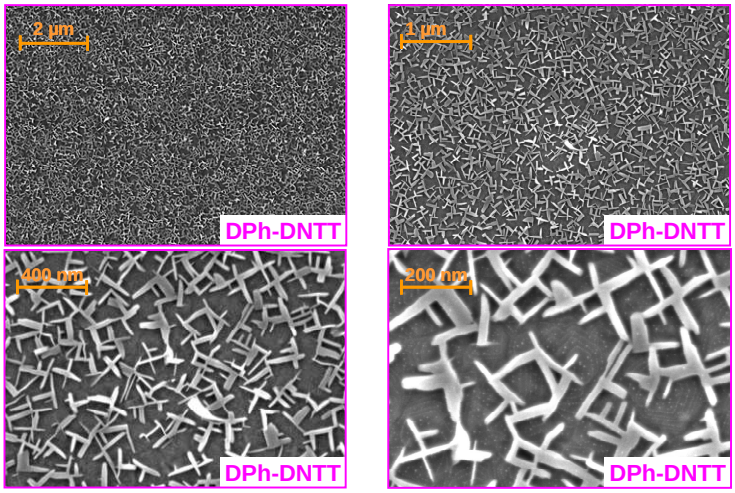

Figure S3. Morphology of vacuum-deposited DPh-DNTT thin-films with higher magnification. The images were obtained by scanning electron microscopy (SEM) with an acceleration voltage of 1.0 to 1.5 kV. Image width (from top left to lower right): 10 µm, 5 µm, 2 µm, 1 µm.

2. Organic thin-film transistors

Table S1. Effective field-effect mobility, threshold voltage, subthreshold swing, transconductance and on/off current ratio of pentacene, DNTT, C_{10}-DNTT and DPh-DNTT TFTs with three representative channel lengths (100 µm, 10 µm, 1 µm; channel width: 200 µm) in the**linear regime (V_{DS} = -0.1 V)**.

Semiconductor	Channel length (µm)	Effective field-effect mobility (cm^2/Vs)	Threshold voltage (V)	Subthreshold swing (mV/decade)	On/off current ratio
Pentacene	100	1.3	-1.31	142	10^5
	10	0.6	-1.35	118	10^6
	1	0.14	-1.14	125	10^5
DNTT	100	3.7	-1.54	88	10^6
	10	1.6	-1.37	85	10^6
	1	0.17	-1.38	100	10^6
C_{10}-DNTT	100	5.4	-0.68	87	10^6
	10	1.5	-0.60	106	10^6
	1	0.17	-0.74	118	10^6
DPh-DNTT	100	6.2	-1.16	90	10^6
	10	2.4	-1.21	96	10^6
	1	0.34	-1.12	101	10^7

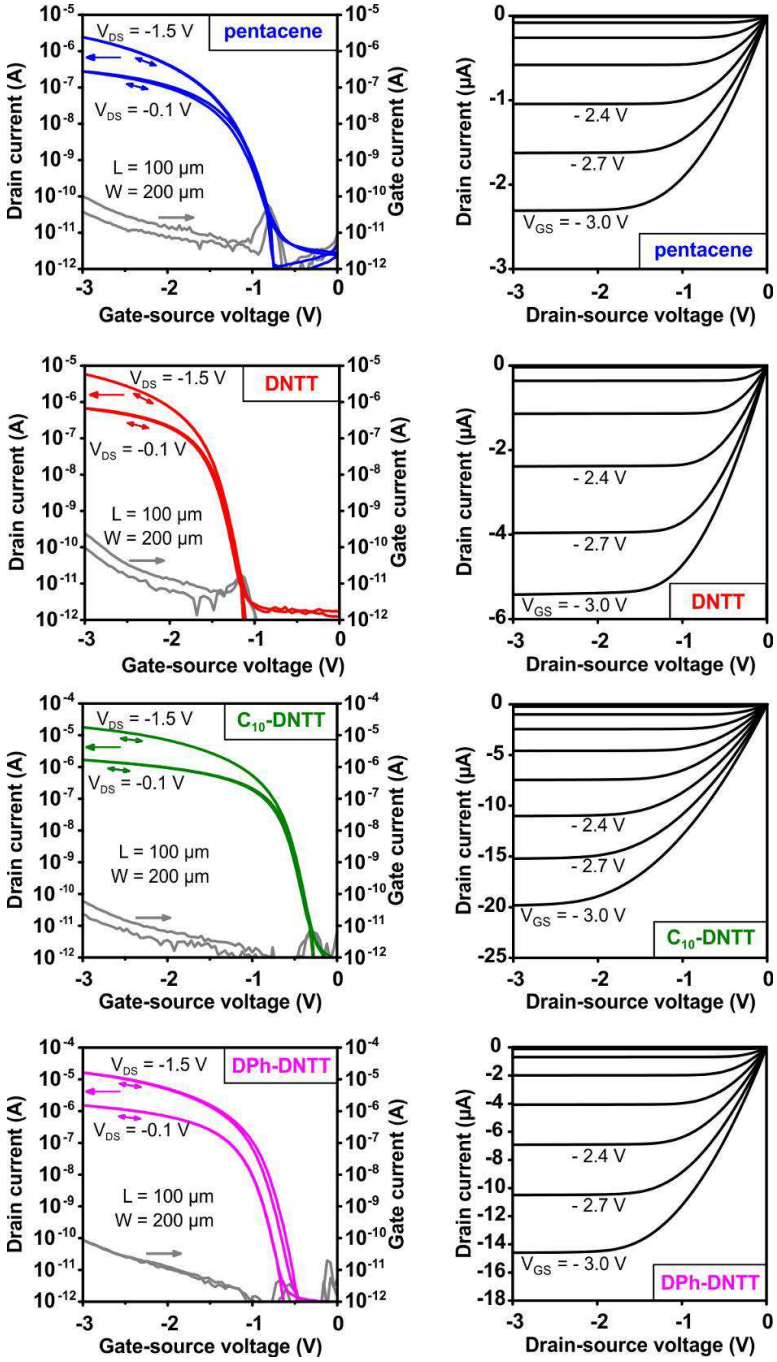

Figure S4. Measured transfer characteristics in the linear (V_{DS} = -0.1 V) and in the saturation regime (V_{DS} = -1.5 V) and output characteristics of a pentacene TFT (blue), a DNTT TFT (red), a C_{10}-DNTT TFT (green) and a DPh-DNTT TFT (purple), all having a channel length of 100 µm and a channel width of 200 µm.

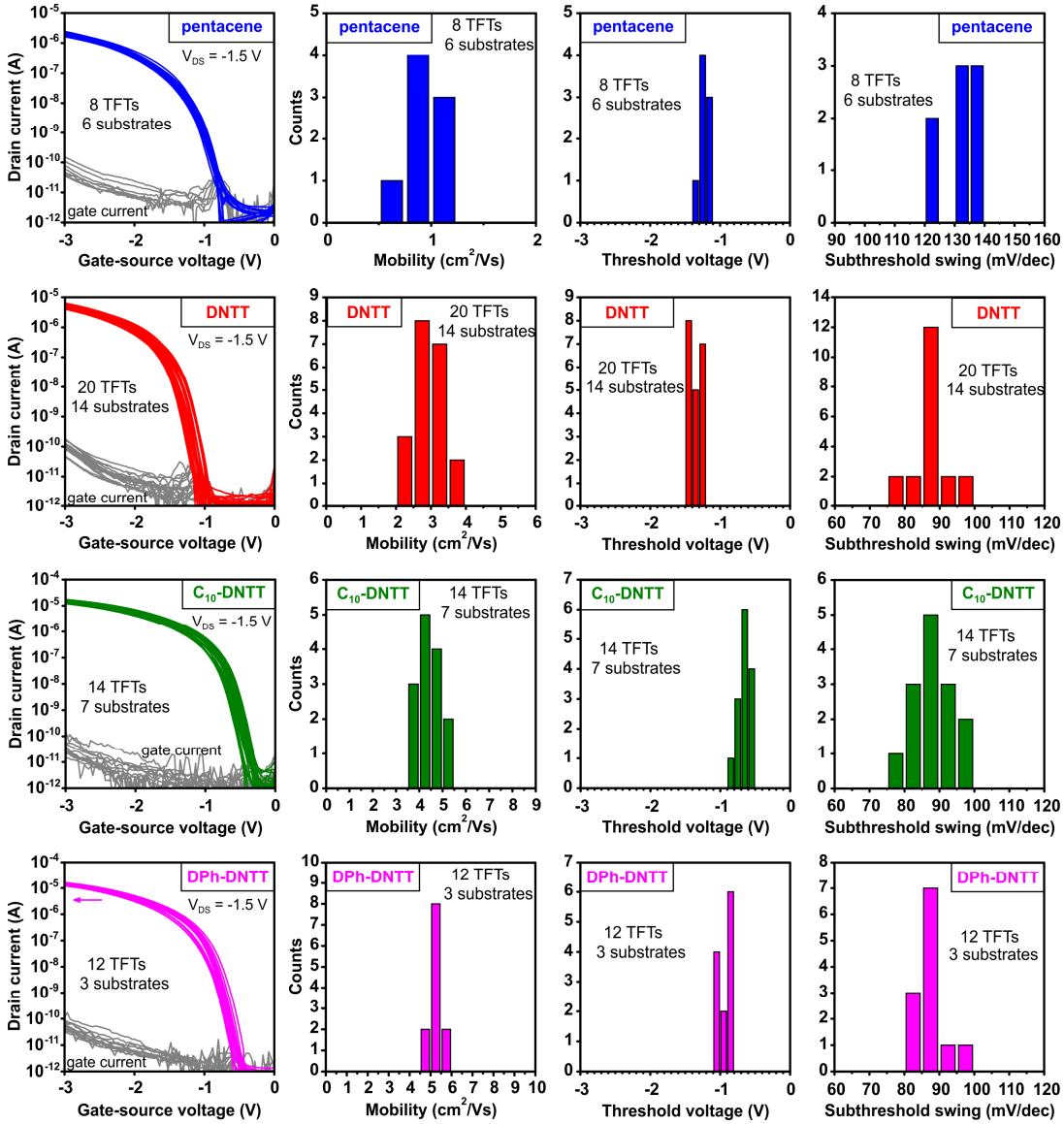

Figure S5. Parameter variation of 44 TFTs fabricated on 30 different substrates over a period of three years (channel length: 100 µm; channel width: 200 µm).

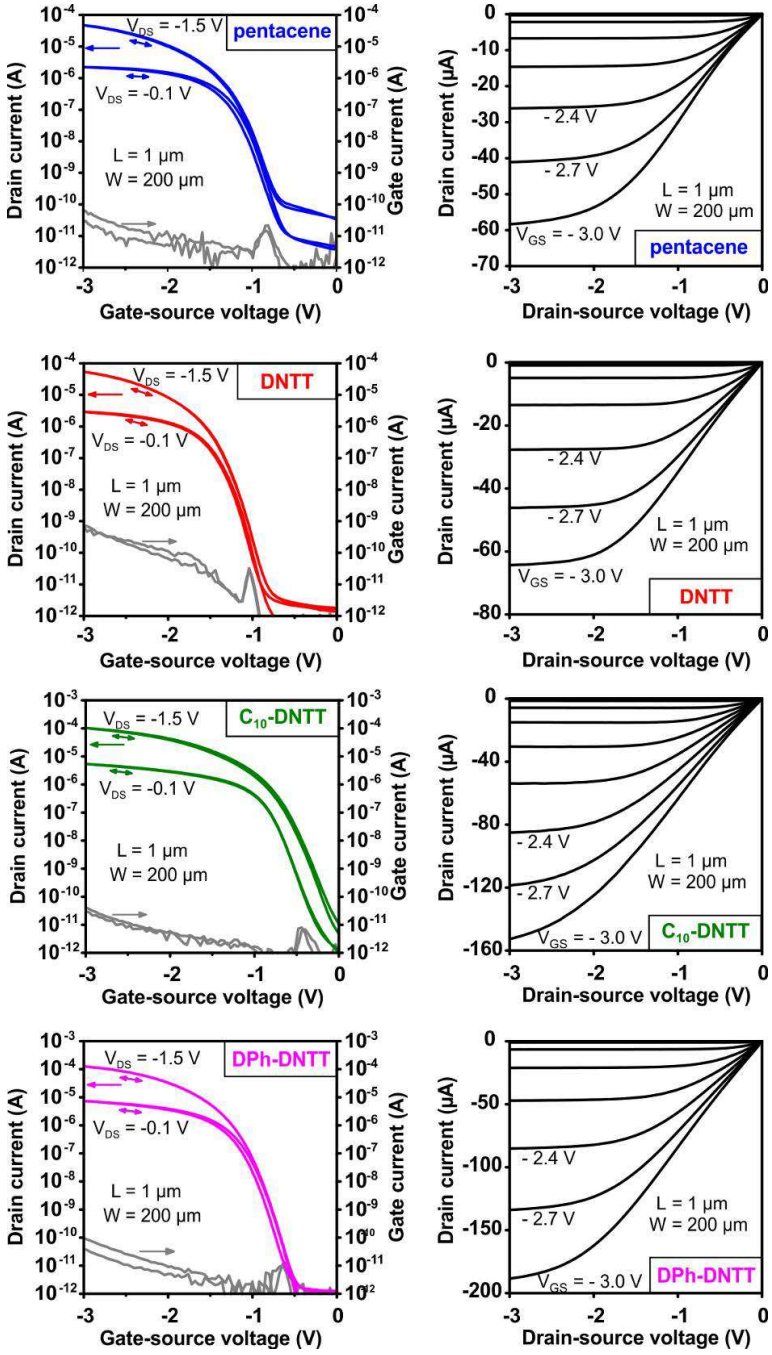

Figure S6. Measured transfer characteristics in the linear (V_{DS} = -0.1 V) and in the saturation regime (V_{DS} = -1.5 V) and output characteristics of a pentacene TFT (blue), a DNTT TFT (red), a C_{10}-DNTT TFT (green) and a DPh-DNTT TFT (purple), all having a channel length of 1 µm and a channel width of 200 µm.

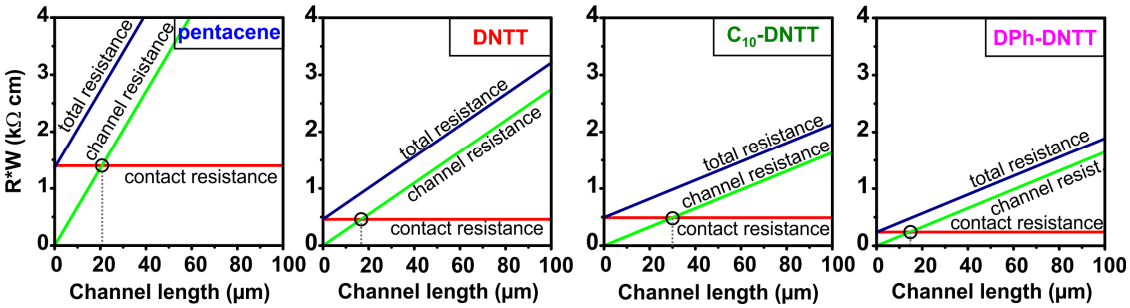

Figure S7. Channel-length dependence of the width-normalized contact resistance (red), the width-normalized channel resistance (green) and the width-normalized total resistance (black) for pentacene, DNTT, C_{10}-DNTT and DPh-DNTT TFTs (V_{GS}-V_{th} = -1.5 V). The sheet resistance equals the slope of the green line ($W \cdot R_{channel} = f(L) = L \cdot R_{sheet}$). $L_{1/2}$ (dotted line) is defined as the channel length at which $R_C = R_{channel}$.

3. Gate-dielectric capacitance measurements

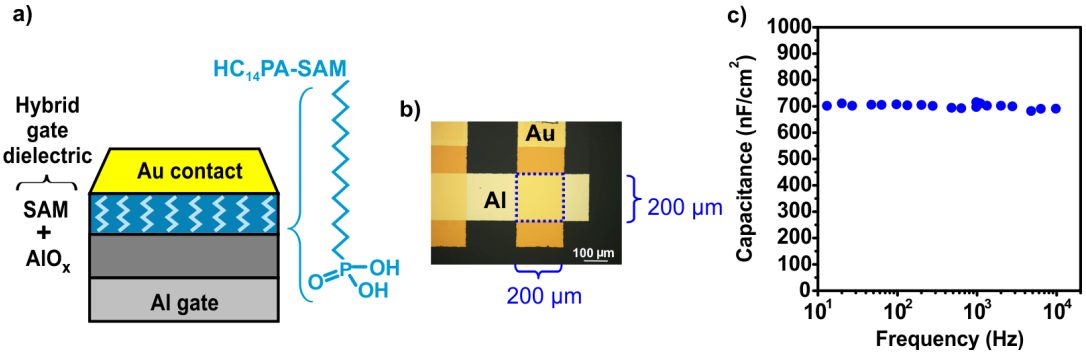

Figure S8. a) Schematic cross-section of the metal-insulator-metal structures on which the capacitance of the hybrid AlO_x/SAM gate dielectric was measured.
b) Optical micrograph of a Al/AlO_x/SAM/Au capacitor structure with shadow-mask patterned Al bottom and Au top electrodes that define a capacitor with an area of 200 µm × 200 µm.
c) Measured capacitance per unit area of the AlO_x/SAM gate dielectric as a function of frequency.